

The Art of Imitation: Learning Long-Horizon Manipulation Tasks from Few Demonstrations

Jan Ole von Hartz, Tim Welschehold, Abhinav Valada, and Joschka Boedecker

Abstract—Task Parametrized Gaussian Mixture Models (TP-GMM) are a sample-efficient method for learning object-centric robot manipulation tasks. However, there are several open challenges to applying TP-GMMs in the wild. In this work, we tackle three crucial challenges synergistically. First, end-effector velocities are non-Euclidean and thus hard to model using standard GMMs. We thus propose to factorize the robot’s end-effector velocity into its direction and magnitude, and model them using Riemannian GMMs. Second, we leverage the factorized velocities to segment and sequence skills from complex demonstration trajectories. Through the segmentation, we further align skill trajectories and hence leverage time as a powerful inductive bias. Third, we present a method to automatically detect relevant task parameters *per* skill from visual observations. Our approach enables learning complex manipulation tasks from just five demonstrations while using only RGB-D observations. Extensive experimental evaluations on RLbench demonstrate that our approach achieves state-of-the-art performance with 20-fold improved sample efficiency. Our policies generalize across different environments, object instances, and object positions, while the learned skills are reusable.

I. INTRODUCTION

Learning robot manipulation tasks from a handful of demonstrations is a challenging problem [1], [2]. This problem is exacerbated when learning only from visual observations and aiming to generalize across task instances. Deep learning approaches can be parameterized flexibly and generalize well, but usually require hundreds of demonstrations or multiple stages [3]. Leveraging compact observation spaces, such as scene keypoints, alleviates the problem, but does not resolve it entirely [4]. In contrast, Gaussian Mixture Models (GMMs) [5] can be learned from only a handful of demonstrations. Various extensions to the GMM framework exist to enable generalization across task instances. For example, Task-Parameterized GMMs (TP-GMM) [6] generalize by modeling the set of demonstrations from the perspective of multiple relevant coordinate frames, called *task-parameters*.

Current methods based on TP-GMMs exhibit a set of serious limitations. First, velocity information is often important for effectively modeling robotic tasks. However, velocities are best expressed by their direction and magnitude, and are poorly represented using Euclidean approaches. As GMMs typically assume Euclidean data, velocity information is difficult to model using TP-GMMs [7]. Second, GMMs suffer from the *curse of dimensionality*, i.e. they scale poorly to both high-dimensional data and long trajectories. Both

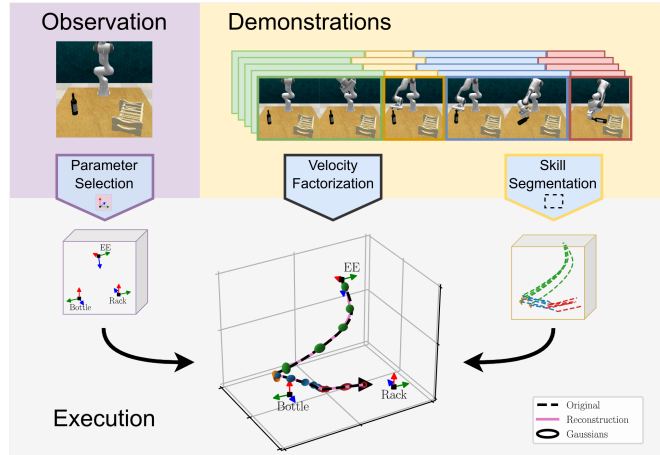


Fig. 1: *TAPAS-GMM*: Task Auto-Parameterized And Skill Segmented GMM learns task-parameterized manipulation policies from only a handful of complex task demonstrations. First, we segment the full task demonstrations into the involved skills. For each segment, we then automatically select the relevant task parameters and learn a Riemannian Task-Parameterized Hidden Markov Model (TP-HMM). The skill models can be cascaded and reused flexibly. To enable modeling of the robot’s end-effector velocity, we further leverage a novel action factorization and Riemannian geometry.

are crucial drawbacks in a robotics context. On the one hand, the dimensionality of the TP-GMM scales linearly with the number of task parameters. On the other hand, even seemingly simple tasks such as *pick and place* can be too long and complex to fit. Third, tasks often consist of multiple skills such as *pick up the bottle*. These skills might not be temporally aligned across demonstrations, rendering the data distribution even more complex. Fourth, when learning from visual observations, generating a set of candidate task parameters is an open problem [8], [9]. In practice, object tracking systems are used [10], but this hardware dependency severely limits the model’s applicability. Finally, the task-parameter selection is crucial for the resulting model quality. However, existing approaches for selecting among a set of candidates also suffer from the curse of dimensionality [11].

We propose Task Auto-Parameterized And Skill Segmented GMM *TAPAS-GMM*, illustrated in Fig. 1. Our method addresses this set of challenges synergistically. First, we propose to refactorize the robot’s velocity into direction and magnitude to better capture the underlying data distribution. We then model both using Riemannian GMMs [10] which are not constrained by the Euclidean assumptions. Second, we segment the task demonstrations into skills using the velocity information. The segmentation both aligns the trajectories temporally and enables learning skill models with shorter trajectories and lower data dimensionality. Additionally, the

temporal alignment enables us to use time as a powerful inductive bias for the initialization of our model. If the trajectories are aligned, then simple binning of the trajectories over the time dimension yields an excellent initialization. Third, we use a pretrained visual encoder network [12] to generate object keypoints that generalize across object instances and task environments [4]. This way, we generate a set of *candidate* task parameters from RGB-D observations. Finally, for selecting the task-relevant parameters from these candidates, we offer an approach that scales well to large numbers of candidates. Our proposed solutions have synergistic effects. For example, combining our parameter selection and skill segmentation further reduces the data dimensionality, as a given task parameter is often only relevant for *some* skill and not the whole long-horizon task.

We evaluate our method on a diverse set of manipulation tasks, both in RL Bench [13] and on a real robot, including articulated objects, as well as high-precision, and long-horizon tasks. We experimentally disentangle policy learning and representation learning, as well as ablating the major components of our approach. *TAPAS-GMM* learns long-horizon manipulation policies from as little as five demonstrations. We show generalization across object positions, object instances, visual clutter, and task environments. Finally, we demonstrate how the learned skills can be recombined in novel ways.

In summary, our main contributions are

- 1) a novel action factorization to effectively model end-effector velocities using Task-Parameterized Gaussian Mixture Models.
- 2) a new velocity-based approach to segmenting complex demonstration trajectories into skills.
- 3) an approach that efficiently extracts and selects task parameters per skill from visual observations.
- 4) rigorous evaluation of our approach’s ability to overcome the problems outlined above, and its efficacy for policy learning, both in simulation and on a real robot.
- 5) We make the code and models publicly available at <http://tapas-gmm.cs.uni-freiburg.de>.

The supplementary material is appended at the end of this paper.

II. RELATED WORK

Parameterized Motions: GMMs [5] learn robotic manipulation tasks from only a handful of demonstrations. Popular alternatives are Dynamic Motion Primitives (DMP) [14] and Probabilistic Motion Primitives (ProMP) [15]. However, all three methods require additional techniques to adapt to novel task instances. Calinon *et al.* [6] identify three classes of adaptation methods: model database, parametric, and multi-stream, to which we amend two-stage and point-based approaches. Model database approaches [16] learn one model per demonstration, that they retrieve and combine based on the associated parameters. In contrast, parametric models [17] learn a single, parameterized model. Two-stage approaches first learn a model encoding a primitive motion, that they adapt in a second stage, e.g. using reinforcement

learning [18] or Wasserstein gradients [19]. However, this requires a second online learning phase. Whereas, multi-stream approaches [20] model the same set of demonstrations from the perspective of multiple coordinate frames, called *task-parameters*. They generalize via the transformation and combination of these local models. Task-parameterized Gaussian Mixture Models (TP-GMM) [6], [10], [21] are multi-stream methods, leveraging a single expectation-maximization procedure. Finally, point-based approaches [9], [22] warp the underlying model to explicit endpoints and waypoints.

TP-GMMs estimate the relevance of a task parameter for a given observation from the variance observed in the task demonstrations. Consequently, they generalize poorly when given fewer than a handful of demonstrations [9]. In contrast, directly editing waypoints [9], [22] is feasible for just a single demonstration. However, task parameters can be extracted from visual observations [23], while defining waypoints may require significant engineering effort. Moreover, by using multiple demonstrations, TP-GMMs approximate the full trajectory distribution suited to solve a given task, instead of assuming the optimality of a single demonstration. Most importantly, TP-GMMs can be extended to model rotations [10], which are required to effectively solve many robotic manipulation tasks. Whereas, both Elastic-DS [9] and KMP [22] are only defined for Euclidean spaces.

Parameter Selection: Task-parameters are usually “assumed to be known or given during demonstrations” [9]. This requires “the experimenter to provide an initial set of [potentially relevant candidate] frames” [8]. Given a set of candidate frames, their respective relevance for a given demonstration can be estimated [24]. However, current approaches fit a joint model to all candidate frames [24]. Hence, they suffer from the *curse of dimensionality*, which our method avoids. Furthermore, automatically generating an initial set of candidate frames is an open problem [8], [9]. In practice, infrared motion tracking devices are manually attached to relevant objects [10], limiting the practical applicability of these methods. In contrast, we propose to automatically identify candidate task parameters from visual observations and to select those relevant to the task at hand. This enables instance-level generalization across objects and applications in novel and changing environments.

Sample-Efficient Long-Horizon Manipulation: GMMs are typically used to model full trajectories [18], with some work focusing on solving long-horizon tasks by sequencing learned GMMs in a bottom-up manner [21]. In contrast, we focus on directly learning long-horizon tasks by segmenting and sequencing skills *top-down* from complex task demonstrations. Some deep learning based approaches [25], [26] simplify long-horizon problems, by only predicting a set of key poses and using motion planning in between. However, by throwing away the trajectory information between key poses, they cannot produce constraint motions such as opening a cabinet. Moreover, they can only predict key poses in the demonstrated order, whereas our approach further produces a set of reusable and re-combinable skills.

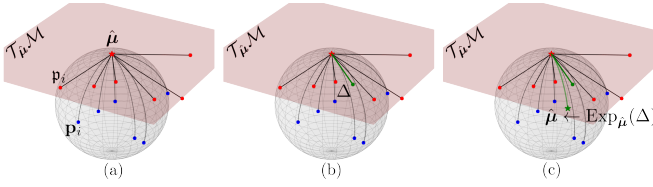


Fig. 2: Iterative likelihood maximization for finding a Riemannian center of mass. (a) Given a current estimate $\hat{\mu}$ (\star), project the data points p_i (\bullet) in the tangent space (\bullet) as $p_i = \text{Log}_{\hat{\mu}}(p_i)$. (b) Compute an update Δ in tangent space (\bullet) and (c) project it back onto the manifold (\star) using $\text{Exp}_{\hat{\mu}}$. Iterate until convergence. Source: Adapted from [10].

III. BACKGROUND

In this section, we summarize foundational work on Gaussian Mixture Models for robotic manipulation, including Hidden Markov Models (HMM), task-parameterization, and Riemannian GMMs. We provide additional details including full equations in Sec. S.1 of the supplementary material.

A. Gaussian Mixture Model

A Gaussian Mixture Model (GMM) with K Gaussian components is defined as $\mathcal{G} = \{\pi_k, \mu_k, \Sigma_k\}_{k=1}^K$. μ_k and Σ_k denote the k -th component's mean and covariance matrix and π_k denotes its prior probability. In the context of Learning from Demonstrations, GMMs are employed to estimate the joint distribution of a disjoint set of input variables \mathcal{I} and output variables \mathcal{O} , from a set of task demonstrations \mathcal{D} as

$$p_{\mathcal{G}}(\mathcal{D}) = p(\mathcal{I}, \mathcal{O} | \mathcal{G}) = \sum_{k=1}^K \pi_k \cdot \mathcal{N}(\mathcal{I}, \mathcal{O} | \mu_k, \Sigma_k). \quad (1)$$

We define $\mathcal{D} = \{\{z_t^n\}_{t=1}^T\}_{n=1}^N$, where $z \in \mathcal{I} \cup \mathcal{O}$, while t indexes time and n the demonstration. We use Expectation Maximization (EM) to maximize the probability of \mathcal{D} under \mathcal{G} . For inference, we employ Gaussian Mixture Regression (GMR) [27] to estimate the conditional density

$$p_{\mathcal{G}}(\mathcal{O} | \mathcal{I}) = \sum_{k=1}^K \pi_k^{\mathcal{I}} \cdot \mathcal{N}(\mathcal{O} | \mu_k^{\mathcal{O}|\mathcal{I}}, \Sigma_k^{\mathcal{O}|\mathcal{I}}). \quad (2)$$

Next, we discuss the choice of input and output variables.

B. Time-Driven vs. State-Driven Models

There are at least two ways to model robotic GMM policies: time-driven and state-driven. Let ξ denote the robot's end-effector pose. Time-driven GMMs model the robot's state conditional on time: $p(\xi | t)$, i.e. $\mathcal{I} = \{t\}$ and $\mathcal{O} = \{\xi\}$. As they do not model the robot's velocity, we post-process the predictions to ensure compliance with the robot's velocity limits, e.g. using TOPPRA [28].

State-driven GMMs model the robot's velocity given its current state: $p(\dot{\xi} | \xi)$, i.e. $\mathcal{I} = \{\xi\}$ and $\mathcal{O} = \{\dot{\xi}\}$, which also captures the robot's velocity limits. However, velocities are harder to model because they are non-Euclidean. Specifically, velocity trajectories are usually less smooth and have more multimodalities than state trajectories. Moreover, velocity errors can aggregate over time. Additionally, deployment on a robot can require time-independence of the policy, e.g. to effectively deal with disturbances. We evaluate these aspects experimentally in Sec. V-B.

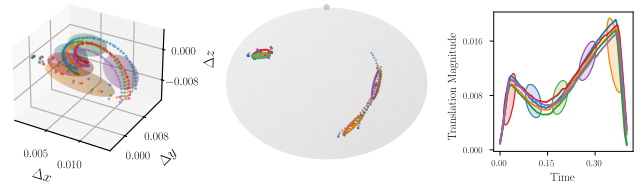


Fig. 3: Velocity trajectories from the first skill in StackWine. *Left*: The velocities are difficult to cluster in Euclidean space. *Middle*: S^2 models the movement direction. *Right*: The associated action magnitudes.

C. Hidden Markov Model

The GMM's posterior $p_{\mathcal{G}}(\mathcal{O} | \mathcal{I})$ in Eq. (2) only depends on the priors $\pi_k^{\mathcal{I}}$ and the conditioned Gaussians, not on any previous observations. The Hidden Markov Model (HMM) [29] augments the GMM by associating each Gaussian with a state k and modeling the transition probability a_{kl} from state k to state l . I.e. $\mathcal{H} = \{\pi_k, \{a_{kl}\}_{l=1}^K, \mu_k, \Sigma_k\}_{k=1}^K$. This helps the model to differentiate between components that are close together in the input space, yet model different parts of a task or movement. For a sequence of observations $\{i_t\}_{t=0}^T$, the computation of the prior thus changes to

$$\pi_k^{i_t} = \frac{(\sum_{l=1}^K \pi_l^{i_{t-1}} a_{lk}) \mathcal{N}(i_t | \mu_k^{\mathcal{I}}, \Sigma_k^{\mathcal{I}})}{\sum_{m=1}^K [(\sum_{l=1}^K \pi_l^{i_{t-1}} a_{lm}) \mathcal{N}(i_t | \mu_m^{\mathcal{I}}, \Sigma_m^{\mathcal{I}})]}. \quad (3)$$

For clarity, we continue referring to our models as GMMs, even though *all* of them use the HMM extension.

D. Task-Parameterization

Task-Parameterized GMMs [6] model the movement from the perspective of multiple coordinate frames, called *task-parameters*, in one joint GMM [10]. These frames are attached to task-relevant objects, but may also include the robot's frame and a world frame. Let $x(f)$ denote the end-effector position in the frame of task-parameter f . We discuss the extension to full poses $\xi(f)$ in Sec. III-E. For the time-driven model and F task-parameters, we model $\mathcal{I} = \{t\}$ and $\mathcal{O} = \{x(f)\}_{f=1}^F$. In contrast, for the state-driven model, we define $\mathcal{I} = \{x(f)\}_{f=1}^F$ and $\mathcal{O} = \{\dot{x}(f)\}_{f=1}^F$. Akin to the vanilla GMM, we fit all parameters jointly using EM. Next, we compute the per-frame *marginal* model for each frame $1 \leq f \leq F$. For example, in the state-driven case we estimate

$$p_f(\mathcal{I}, \mathcal{O} | \mathcal{G}) = p(x(f), \dot{x}(f) | \mathcal{G}). \quad (4)$$

To adapt to a given set of task parameters $\Theta = \{A_f, b_f\}_{f=1}^F$, we transform the per-frame marginals to the world frame. b_f denotes the origin of frame f and A_f its rotation matrix. Let

$$p_f(\mathcal{I}, \mathcal{O} | \mathcal{G}) = \left\{ \pi_k^f, \mu_k^f, \Sigma_k^f \right\}_{k=1}^K \quad (5)$$

be a marginal. Then its transformed marginal is given by

$$p_f(\mathcal{I}, \mathcal{O} | \mathcal{G}, \Theta) = \left\{ \pi_k^f, \hat{\mu}_k^f, \hat{\Sigma}_k^f \right\}_{k=1}^K \quad (6)$$

$$\hat{\mu}_k^f = A_f \mu_k^f + b_f$$

$$\hat{\Sigma}_k^f = A_f \Sigma_k^f A_f^T.$$

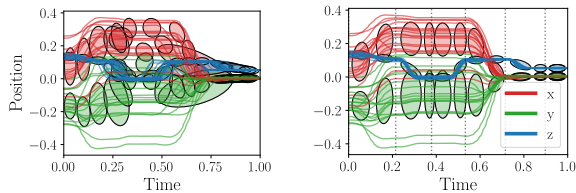


Fig. 4: *Left*: GMM on unaligned demos. *Right*: GMM on aligned demos. Dotted lines indicate segment borders.

Finally, we compose the joint model as

$$p_{\mathcal{G}}(\mathcal{I}, \mathcal{O} | \Theta) = \prod_{f=1}^F p_f(\mathcal{I}, \mathcal{O} | \mathcal{G}, \Theta). \quad (7)$$

We then perform GMR on the joint model as defined in Eq. (2). For an excellent, more detailed overview of TP-GMMs, please refer to [8].

E. Riemannian Manifolds

We model the robot’s end-effector pose $\xi = [\mathbf{x} \ \theta]^T$ on the Riemannian Manifold $\mathcal{M}_{\text{pose}} = \mathbb{R}^3 \times \mathcal{S}^3$. Whereas, GMMs typically assume Euclidean data, the naive Euclidean mean of a set of quaternions is generally not a valid quaternion. Instead of projecting the naive solution back onto the manifold, we solve the problem rigorously using Riemannian geometry [10]. Each Riemannian manifold \mathcal{M} is differentiable, i.e., at each point \mathbf{x} , it has a tangent space $\mathcal{T}_{\mathbf{x}}\mathcal{M}$, that is a real vector space. The *logarithmic map* $\text{Log}_{\mathbf{x}} : \mathcal{M} \rightarrow \mathcal{T}_{\mathbf{x}}\mathcal{M}$ straightens the manifold’s curvature while preserving geodesic distance. The inverse is the *exponential map* $\text{Exp}_{\mathbf{x}} : \mathcal{T}_{\mathbf{x}}\mathcal{M} \rightarrow \mathcal{M}$. Both depend on the *base* \mathbf{x} , at which they are applied. Following Zeestraten [10], we formulate all previously Euclidean operations in EM and GMR as non-linear Maximum Likelihood Estimation problems. For example, to compute the center of mass μ of a Riemannian Gaussian, we initialize the procedure with some estimate $\hat{\mu}$ and solve the MLE using the following iterative process.

- 1) Tangent project the data using $\text{Log}_{\hat{\mu}}$.
- 2) Update $\Delta \in \mathcal{T}_{\hat{\mu}}\mathcal{M}$ using a Gauss-Newton step.
- 3) Back-project the update $\hat{\mu} \leftarrow \text{Exp}_{\hat{\mu}}(\Delta)$.

In practice, only a handful of iterations suffice for $\hat{\mu}$ to converge. Fig. 2 illustrates the procedure. All other operations such as conditioning can be solved in a similar manner [10]. Finally, we use the concept of parallel transport to implement the affine frame transformations in Eq. (6) for the full pose. We provide additional details in Sec. S.2 of the supplementary material. Zeestraten provides an excellent introduction into TP-GMMs on Riemannian Manifolds [10]. Note, that we found parallel transport to sometimes introduce unwanted correlations into the model’s covariance, leading to faulty predictions. We discuss the problem and our proposed solution in detail in Sec. S.3 of the supplementary material.

IV. TECHNICAL APPROACH

We aim to learn robot manipulation policies that generalize to unseen task instances from just five demonstrations. To generalize across object instances and be independent of object-tracking hardware, the task parameters should be

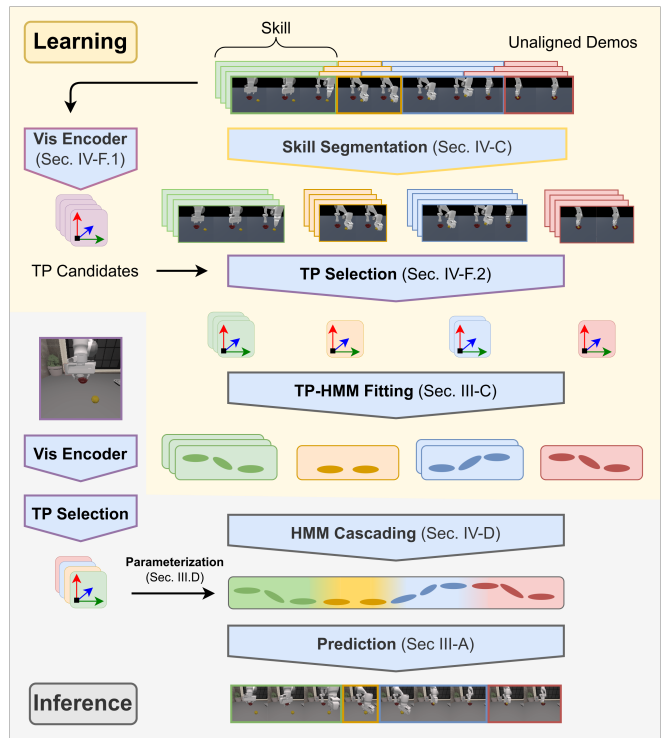


Fig. 5: Overview of our approach. *Learning*: First, we segment a set of complex task demonstrations with unaligned skills. Next, we generate a set of candidate task parameters from visual observations and select the relevant parameters for each segment. Finally, we fit one Task-Parameterized Hidden Markov Model (TP-HMM) per segment. *Inference*: To make a prediction for new visual observations, we again extract the set of task parameters and select the task parameters determined during the learning phase. We then cascade the segment TP-HMMs.

extracted from RGB-D observations. For fast and easy data collection, complex tasks should automatically be segmented into their atomic skills. The method should not require one collection phase per atomic skill and should be able to construct novel sequences that were not demonstrated.

We present *TAPAS-GMM*: Task-Parameterized and Skill Segmented GMM. Our approach is based on Riemannian Task-Parameterized Hidden Markov Models. To effectively model velocity data, we propose a novel factorization. We then segment skills from complex demonstrations to temporally align the demonstrations and to learn skill models that we can sequence and reuse later. Finally, we propose an approach to automatic task parameterization and combine these techniques in a synergistic manner. Fig. 5 summarizes our approach. We now introduce the components in turn.

A. Action Factorization

In Sec. III-B, we discussed that solving manipulation tasks can require modeling the end-effector’s velocity $\dot{\xi}$ and not only its pose ξ , e.g. if time-independence is required. Fig. 3 illustrates that naively modeling $\dot{\xi}$ on the manifold $\mathcal{M}_{\text{pose}} = \mathbb{R}^3 \times \mathcal{S}^3$ (introduced in Sec. III-E) is difficult because velocities are not Euclidean. Instead, they are vector quantities defined by a direction and magnitude. We therefore propose to factorize the end-effector velocity $\dot{\xi}$ as

$$\dot{\xi} = \begin{bmatrix} \hat{\mathbf{x}} & \hat{\theta} & \|\dot{\mathbf{x}}\| & \|\dot{\theta}\| \end{bmatrix}^T. \quad (8)$$

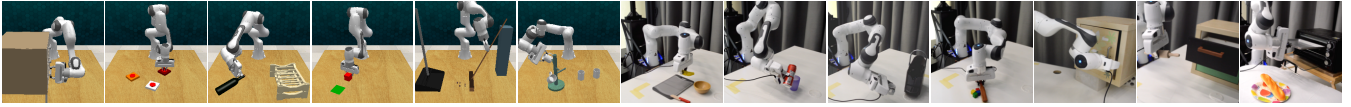


Fig. 6: *Left*: The RL Bench tasks OpenDrawer, PushButtons, StackWine, SlideBlock, SweepToDustpan, and PlaceCups. *Right*: The real-world tasks PickAndPlace, PourDrink, MakeCoffee, SweepBlocks, OpenCabinet, StoreInDrawer, and BakeBread.

The translation direction $\hat{\mathbf{x}}$ is the normalized translation vector, whereas $\hat{\boldsymbol{\theta}}$ is the rotation *axis*. Both lie on \mathcal{S}^2 . The translation magnitude $\|\hat{\mathbf{x}}\| \in \mathbb{R}$ is the norm of the translation vector and $\|\hat{\boldsymbol{\theta}}\| \in \mathcal{S}^1$ is the rotation angle. The combined manifold is $\mathcal{M}_{\text{vel}} = \mathcal{S}^2 \times \mathcal{S}^2 \times \mathbb{R} \times \mathcal{S}^1$. For a set F of task parameters, the full manifold of our state-driven TP-GMM is given by

$$\mathcal{M} = (\mathcal{M}_{\text{pose}} \times \mathcal{S}^2 \times \mathcal{S}^2)^F \times \mathbb{R} \times \mathcal{S}^1. \quad (9)$$

Our insight is three-fold. First, in the task-parameterized setting, only the direction of the velocities varies between different fixed coordinate frames, not their magnitude. Thus, we reduce the dimensionality of the problem by modeling the magnitudes globally. Second, because velocities are not Euclidean, their distributions are easier to estimate when factorized. To model the factorized velocities, we leverage the Riemannian toolbox introduced in Sec. III-E. Third, we leverage the isolated velocities to automatically segment complex task trajectories into the involved skills. We found this to drastically improve the quality and transferability of the learned model and discuss it in detail in Sec. IV-C. Fig. 3 illustrates how the velocities are easier to model in the factorized representation. We provide additional details on how to implement the frame transformations for \mathcal{S}^2 in Sec. S.2 of the supplementary material.

B. Gripper Action

Effectively solving manipulation tasks also requires modeling the gripper action. To this end, we add another global action dimension \mathbb{R} , modeling the gripper width, to Eq. (9).

C. Skill Segmentation

Robot manipulation tasks often involve a set of skills. The pick and place task in Fig. 5 consists of four skills. 1) Align the gripper with the first object. 2) Grasp it. 3) Align the first object with the second object. 4) Place the first object. All skills have distinct dynamics, so it is difficult to model them jointly in a single *state*-driven GMM. Furthermore, the skills have different relative durations across task instances, leading to poor temporal alignment across demonstrations. Fig. 4 illustrates that as a consequence they are difficult to model with a single *time*-driven GMM.

Therefore, we propose to automatically segment the full demonstration trajectories into a sequence of skill demonstrations and to learn one model per skill. This allows us to temporally align the skills and to learn local dynamics, specific to the skills. The skill model can be time-driven or state-driven. Furthermore, it allows us to reuse the learned skills by sequencing them in novel ways. Lastly, in Sec. IV-E and Sec. IV-F we discuss its synergistic effects with our initialization strategy and our automatic task-parameterization, respectively. To segment the trajectories, we threshold the

action magnitudes introduced in Sec. IV-A. Observations with near-zero action magnitude yield a set of segmentation point candidates that we then cluster across the set of demonstrations using density-based clustering. Afterward, we fit one TP-HMM per skill.

D. Skill Sequencing and Skill Reuse

We execute a sequence of skills by cascading the associated HMMs. To cascade two HMMs $\mathcal{H}_1, \mathcal{H}_2$, Rozo *et al.* astutely propose to calculate the transition probability a_{ij} between state $i \in \mathcal{H}_1$ and state $j \in \mathcal{H}_2$ using the KL-divergence between the associated Gaussians [21] as

$$a_{ij} \propto \exp(-D_{KL}(\mathcal{N}(\boldsymbol{\mu}_i, \boldsymbol{\Sigma}_i) \parallel \mathcal{N}(\boldsymbol{\mu}_j, \boldsymbol{\Sigma}_j))). \quad (10)$$

In case \mathcal{H}_1 and \mathcal{H}_2 contain different task parameters, we marginalize the Gaussians to their set of common task parameters first. Afterward, we normalize the outgoing probabilities of all states. Computing the KL-divergence can be difficult for Riemannian Gaussians, so we estimate it efficiently using a Monte-Carlo sampling scheme [30]. We employ this procedure iteratively to longer sequences of HMMs. Note that this skill sequencing procedure does not require the skills to be sequenced in the demonstrated order. Instead, it allows us to solve new tasks by reordering and sequencing learned skills. Note further that time-based GMM skills can easily be reversed, either by manipulating the mean and covariance matrices or by reversing the time signal. In combination, this allows us to create a rich set of new task policies, which we demonstrate in Sec. V-D.

E. Time-Based Initialization

EM is not guaranteed to converge to the *global* optimum, but only to a local optimum [10]. Consequently, its initialization is of critical importance. *K*-means clustering is popular but does not guarantee a global optimum either [10]. We efficiently segment the trajectories along the time dimension using *K*-bins. Fig. 4 illustrates that complex task demonstrations are usually not aligned temporally. However, our skill segmentation proposed in Sec. IV-C aligns them, yielding a good initialization for EM. The combination of skill segmentation and time-based initialization enables the EM procedure to arrive at good local optima, while also achieving significantly faster convergence. Next, we discuss how we leverage it to efficiently select task parameters, too.

F. Task-Parameterization

Previous work has usually assumed groundtruth access to relevant task-parameters [8], [9] or used infrared motion tracking devices [10], both of which restrict the applicability of the method. We therefore propose an approach to automatically select the relevant task parameters from RGB-D observations.

TABLE I: Success rates of the learned policies in simulated tasks. Results for 3D Diffuser Actor were reported by the authors.

Demonstrations	Method	Task					
		OpenDrawer	PushButtons	StackWine	SlideBlock	SweepToDustpan	PlaceCups
100	3D Diffuser Actor [31]	0.90	0.98	0.93	0.98	0.84	0.24
	Diffusion Policy [32]	0.96	0.00	0.42	0.31	0.32	0.00
	LSTM [33]	0.00	0.06	0.00	0.00	0.00	0.00
5	Diffusion Policy	0.16	0.00	0.00	0.05	0.40	0.00
	LSTM	0.00	0.00	0.00	0.00	0.00	0.00
	TAPAS-GMM (Ours)	0.90	1.00	1.00	0.95	1.00	0.75

TABLE II: Policy success without task-parameter selection or skill segmentation. TP-GMM uses neither. The other models ablate one factor each.

	OpenDrawer	SlideBlock	PlaceCups
TAPAS-GMM (Ours)	0.90	0.95	0.75
└ w/o segmentation	0.06	0.68	0.00
└ w/o TP selection	0.62	0.66	0.03
└ Global TP selection	0.62	0.66	0.10
TP-GMM	0.05	0.64	0.00

Moreover, different skills in the same task require different information, e.g., in *pick and place*, the picking skill is often independent of the placing site. Modelling the full task using both task parameters is not only more computationally expensive but also leads to worse task performance. Hence, our parameter selection method has a synergistic effect with the skill segmentation proposed in Sec. IV-C. We offer a modular two-staged approach to candidate generation based on visual features and task-parameter selection based on statistical considerations. Both operate independently of each other, rendering them straightforward to substitute.

1) *Candidate Generation*: Various methods exist for extracting task parameters from visual observations [23]. Due to their generalization capabilities, we build on recent advances in 3D scene keypoints [4] and leverage a DINO vision transformer [12]. We sample a set of reference descriptors from the embedding of the first image observation of task demonstrations, either manually in a GUI or automatically using SAM-generated object masks [34]. The associated keypoints constitute the set of candidate task parameters. We then localize them in each demonstration by establishing correspondences via the embedding distances [4], [12].

2) *Candidate Selection*: We select task parameters *per skill* based on how well they explain the set of demonstrations. For each skill and candidate frame, we first fit a single-frame model. We only perform the time-based initialization described in Sec. IV-E and not the full EM to ensure temporal alignment across candidates and to speed up the procedure. We then estimate the relative relevance of the per-frame models using the determinants of their Gaussian precision matrices, a metric astutely proposed by Alizadeh *et al.* [11]. Due to the temporal alignment, the relative precision over Gaussian components yields the relative relevance of the candidate frames over time. By calculating the maximum over all Gaussian components, we select all frames that are relevant *at some point* in the segment. Let $(\Sigma_k^f)^{-1}$ denote the k -th component’s precision matrix in the model of frame f .

For C candidate frames with K Gaussians, we estimate

$$\omega(f) = \max_{k=1}^K \frac{\det(\Sigma_k^f)^{-1}}{\sum_{c=1}^C \det(\Sigma_k^c)^{-1}} \quad (11)$$

and select all frames f over some threshold $\omega(f) > \tau$.

In contrast, Alizadeh *et al.* fit a joint model to all candidates and the full task trajectory and calculate the relative precision during trajectory reconstruction [11]. Our per-skill single-frame approach scales to long-horizon tasks and large sets of candidate parameters while the temporal alignment eliminates the need for a reconstruction phase.

V. EXPERIMENTAL RESULTS

We first evaluate the efficacy of *TAPAS-GMM* for policy learning on a set of challenging manipulation tasks from the well established RL Bench benchmark [13] and ablate the major components of our method. Afterward, we compare time-driven and state-driven policies on custom tasks implemented in ManiSkill2 [35]. Finally, we verify our results on a real robot and demonstrate our method’s generalization capabilities. Fig. 6 illustrates the evaluated RL Bench tasks and real world tasks. Additional details for all the experiments are provided in Sec. S.4 of the supplementary material.

A. Time-Driven Policy Learning in Simulation

We compare against LSTM [33] and Diffusion Policy [32] baselines trained with either 100 or 5 demonstrations. In contrast, *TAPAS-GMM* is only trained on five demonstrations. To experimentally disentangle policy learning and representation learning, we use groundtruth object poses as inputs for the baselines and as *candidate* task parameters for *TAPAS-GMM*. We evaluate our proposed *visual* features in Sec. V-C and Sec. V-D. We further compare against 3D Diffuser Actor [31], which at the time of writing is the incumbent on RL Bench. Note that it leverages a 3D scene representation instead of object poses. We evaluate all policies for 200 episodes. Tab. I shows that *TAPAS-GMM* matches or outperforms the SOTA across all tasks while requiring significantly fewer demonstrations. Moreover, in contrast to all baselines, *TAPAS-GMM* scales to more complex long-horizon tasks such as *SweepToDustpan* and *PlaceCups*, without loss in performance. Moreover, unlike the Diffusion Policy and LSTM, it excels when high precision is required, e.g., in *PushButton*.

In Tab. II, we ablate the relevance of task-parameter selection and skill segmentation. The *global* TP selection

TABLE III: Time-driven vs. state-driven **TAPAS-GMM**, with and without disturbance of the rollout. Among the time-driven policies we compare different post-processing strategies. Among the state-driven policies, we compare naive and factorized velocities. Trajectory length is mean and standard deviation.

Driver	Variant	Policy success rate \uparrow				Successful trajectory length [steps] \downarrow			
		Undisturbed		Disturbed		Undisturbed		Disturbed	
		PushBlock	LiftBottle	PushBlock	LiftBottle	PushBlock	LiftBottle	PushBlock	LiftBottle
Time	None	0.85	0.18	0.00	0.00	127 \pm 01	239 \pm 09	-	-
	Threshold	0.96	0.79	0.00	0.00	149 \pm 01	310 \pm 06	-	-
	TOPP-RA	0.35	0.78	0.00	0.17	370 \pm 64	426 \pm 26	-	444 \pm 18
State	Naive	0.76	0.18	0.76	0.19	206 \pm 71	203 \pm 36	266 \pm 59	454 \pm 37
	Factorized	0.83	0.33	0.83	0.32	141 \pm 53	223 \pm 48	228 \pm 47	471 \pm 48

TABLE IV: Real world policy success rates.

	PickAndPlace	PourDrink	MakeCoffee	SweepBlocks	OpenCabinet	StoreInDrawer	BakeBread
LSTM	0.00	0.00	0.00	0.00	0.00	0.00	0.00
Diffusion Policy	0.00	0.00	0.00	0.00	0.00	0.00	0.00
TP-GMM	0.20	0.08	0.00	0.16	0.00	0.68	0.36
TAPAS-GMM (Ours)	1.00	1.00	0.96	0.96	0.92	1.00	0.96

chooses the parameters for the full task jointly, instead of per skill. As hypothesized, the task-parameter selection is more crucial on multi-object tasks with clutter (`PlaceCups`) than on single-object tasks (`OpenDrawer`, `SlideBlock`). Across all tasks, we observe that the initial end-effector frame is irrelevant after aligning the gripper with the object and reduces policy success if still taken into account. Skill segmentation is most crucial if the task is complex (`PlaceCups`) or precise grasps are required (`OpenDrawer`). The large performance gap between *TAPAS-GMM* and all other models on `PlaceCups` highlights the synergistic effect of skill segmentation and parameter selection.

B. Time-Driven vs. State-Driven Policies

We compare the effectiveness of time-driven and state-driven GMMs in Tab. III. To simulate disturbances during policy rollout, we reset the end-effector pose back to the starting pose, around the object contact point in the trajectory. While state-based policies are harder to learn from few demonstrations, they outperform time-based policies when confronted with disturbances due to their time-invariance. Furthermore, our action-factorized policies consistently outperform the naive implementation.

Moreover, time-based GMMs do not take into account the velocity limits of the robot. Consequently, the predicted trajectories might not be feasible and require some post-processing, such as applying TOPP-RA [28] or only stepping the time when the current pose is close enough to the last prediction (thresholding). These post-processing methods have their own strengths and weaknesses. For example, TOPP-RA helps with precise grasping in `LiftBottle` and improves robustness against disturbances, but struggles with the drag of the object in `PushBlock`. In contrast, our state-driven GMMs explicitly model the robot’s velocity distribution in the demonstrations, thus not requiring post-processing. Often, they also produce shorter trajectories. The biggest drawback of state-driven GMMs that we observed experimentally, is their propensity for divergence during inference. Under velocity control, pose errors can accumulate and push the policy

outside the observed state space. From this they often fail to recover, as frequently happens in `LiftBottle`.

C. Real-World Policy Learning

We verify *TAPAS-GMM* capabilities extensively on a real Franka Emika robot. To this end, we construct a range of challenges such as long-horizon tasks up to 1000 time steps (e.g. `MakeCoffee`, `BakeBread`), tasks requiring high precision (e.g. `MakeCoffee`, `BakeBread`), and articulated objects (e.g. `OpenCabinet`, `StoreInDrawer`). All policies are trained on five task demonstrations and evaluated for 25 episodes. We generate candidate task parameters from wrist-camera observations as proposed in Sec. IV-F.1.

The policy success rates in Tab. IV are consistent with the results in our simulated experiments and demonstrate the core advantages of our approach: 1) strong generalization from few demonstrations, 2) handling of articulated objects, and 3) scaling to complex tasks and long horizons. Consistent with our simulated ablation experiment, TP-GMMs struggle with pose accuracy and gripper timing due to locally irrelevant task parameters and poor temporal alignment. Moreover, the deep learning baselines fail to generalize from five demonstrations and do not learn to solve any task instance. In contrast, *TAPAS-GMM* effortlessly scales to long-horizon tasks, without any loss in accuracy or generalization performance.

D. Visual Generalization and Skill Reuse

Prior work has extensively demonstrated the generalization capabilities of keypoints as visual features [4], which our policies inherit through the parameter generation proposed in Sec. IV-F.1. We study the resulting zero-shot generalization capabilities of our policies on `PickAndPlace` and `PourDrink` by evaluating the policy with unseen objects instances, clutter objects, and task environments. We observe strong generalization performance across the board. We further provide qualitative results and discussions in the supplementary video.

Another advantage of *TAPAS-GMM* is that it not only solves *one* task but instead learns skill models, which can be

recombined to solve novel tasks. In the supplementary video, we demonstrate how the segmented skills can be sequenced and reused in novel ways. In particular, the BakeBread task consists of taking the tray out of the oven and placing the bread on it. As an example, we invert and reorder these skills to construct a policy that takes the bread from the tray and inserts the tray into the oven.

VI. CONCLUSION

We present *TAPAS-GMM*, a method for learning complex manipulation tasks from only five demonstrations. By segmenting skills and automatically selecting relevant task parameters per skill, our method scales both to tasks with long horizons and many parameters. Through leveraging visual semantic features, our method further generalizes across object instances, environments, and clutter. Finally, our proposed velocity factorization makes time-invariant task-parameterized policies more effective.

Limitations: *TAPAS-GMM* is vulnerable to some of the core problems of imitation learning. First, it does not reason about the robot’s kinematic limits or object collisions. Second, it requires a decent coverage of the task space to generalize, which can be difficult to achieve on multimodal trajectory distributions, when given only five demonstrations. This shows in the `PlaceCups` task, where workspace limits cause different task instances to require vastly different trajectory shapes. Adding a prior, encoding workspace limits, and object collision probabilities, might alleviate this problem.

REFERENCES

- [1] C. Celemin, R. Pérez-Dattari, E. Chisari, G. Franzese, L. de Souza Rosa, R. Prakash, Z. Ajanović, M. Ferraz, A. Valada, J. Kober *et al.*, “Interactive imitation learning in robotics: A survey,” *Foundations and Trends® in Robotics*, vol. 10, no. 1-2, pp. 1–197, 2022.
- [2] E. Chisari, T. Welschehold, J. Boedecker, W. Burgard, and A. Valada, “Correct me if i am wrong: Interactive learning for robotic manipulation,” *IEEE Robotics and Automation Letters*, 2022.
- [3] N. Heppert, M. Argus, T. Welschehold, T. Brox, and A. Valada, “Ditto: Demonstration imitation by trajectory transformation,” *arXiv preprint arXiv:2403.15203*, 2024.
- [4] J. O. von Hartz, E. Chisari, T. Welschehold, W. Burgard, J. Boedecker, and A. Valada, “The treachery of images: Bayesian scene keypoints for deep policy learning in robotic manipulation,” *IEEE Robotics and Automation Letters*, vol. 8, no. 11, pp. 6931–6938, 2023.
- [5] S. Calinon, F. Guenter, and A. Billard, “On learning the statistical representation of a task and generalizing it to various contexts,” in *Int. Conf. on Robotics and Automation*, 2006, pp. 2978–2983.
- [6] S. Calinon, T. Alizadeh, and D. G. Caldwell, “On improving the extrapolation capability of task-parameterized movement models,” in *Int. Conf. on Intelligent Robots and Systems*, 2013, pp. 610–616.
- [7] S. Sun, H. Gao, T. Li, and N. Figueroa, “Damm: Directionality-aware mixture model parallel sampling for efficient dynamical system learning,” *arXiv preprint arXiv:2309.02609*, 2023.
- [8] S. Calinon, “A tutorial on task-parameterized movement learning and retrieval,” *Intelligent service robotics*, vol. 9, pp. 1–29, 2016.
- [9] T. Li and N. Figueroa, “Task generalization with stability guarantees via elastic dynamical system motion policies,” in *Conf. on Robot Learning*, 2023, pp. 3485–3517.
- [10] M. J. Zeestraten, “Programming by demonstration on riemannian manifolds.” Ph.D. dissertation, University of Genoa, Italy, 2018.
- [11] T. Alizadeh, S. Calinon, and D. G. Caldwell, “Learning from demonstrations with partially observable task parameters,” in *Int. Conf. on Robotics and Automation*, 2014, pp. 3309–3314.
- [12] S. Amir, Y. Gandselman, S. Bagon, and T. Dekel, “Deep vit features as dense visual descriptors,” *arXiv preprint arXiv:2112.05814*, 2021.
- [13] S. James, Z. Ma, D. Rovick Arrojo, and A. J. Davison, “Rlbench: The robot learning benchmark & learning environment,” *IEEE Robotics and Automation Letters*, 2020.
- [14] A. J. Ijspeert, J. Nakanishi, H. Hoffmann, P. Pastor, and S. Schaal, “Dynamical movement primitives: learning attractor models for motor behaviors,” *Neural computation*, vol. 25, no. 2, pp. 328–373, 2013.
- [15] A. Paraschos, C. Daniel, J. R. Peters, and G. Neumann, “Probabilistic movement primitives,” *Advances in neural information processing systems*, vol. 26, 2013.
- [16] T. Matsubara, S.-H. Hyon, and J. Morimoto, “Learning parametric dynamic movement primitives from multiple demonstrations,” *Neural networks*, vol. 24, no. 5, pp. 493–500, 2011.
- [17] A. Pervez and D. Lee, “Learning task-parameterized dynamic movement primitives using mixture of gmm,” *Intelligent Service Robotics*, vol. 11, no. 1, pp. 61–78, 2018.
- [18] I. Nematollahi, E. Rosete-Beas, A. Röfer, T. Welschehold, A. Valada, and W. Burgard, “Robot skill adaptation via soft actor-critic gaussian mixture models,” in *Int. Conf. on Robotics and Automation*, 2022, pp. 8651–8657.
- [19] H. Ziesche and L. Rozo, “Wasserstein gradient flows for optimizing gaussian mixture policies,” *Advances in Neural Information Processing Systems*, vol. 36, 2024.
- [20] S. Calinon, F. Guenter, and A. Billard, “On learning, representing, and generalizing a task in a humanoid robot,” *IEEE Trans. on Systems, Man, and Cybernetics*, vol. 37, no. 2, pp. 286–298, 2007.
- [21] L. Rozo, M. Guo, A. G. Kupcsik, M. Todescato, P. Schillinger, M. Gifftthaler, M. Ochs, M. Spies, N. Waniek, P. Kesper *et al.*, “Learning and sequencing of object-centric manipulation skills for industrial tasks,” in *Int. Conf. on Intelligent Robots and Systems*, 2020, pp. 9072–9079.
- [22] Y. Huang, L. Rozo, J. Silvério, and D. G. Caldwell, “Kernelized movement primitives,” *The Int. Journal of Robotics Research*, vol. 38, no. 7, pp. 833–852, 2019.
- [23] E. Chisari, N. Heppert, T. Welschehold, W. Burgard, and A. Valada, “Centergrasp: Object-aware implicit representation learning for simultaneous shape reconstruction and 6-dof grasp estimation,” *arXiv preprint arXiv:2312.08240*, 2023.
- [24] T. Alizadeh and M. Malekzadeh, “Identifying the relevant frames of reference in programming by demonstration using task-parameterized gaussian mixture regression,” in *IEEE/SICE Int. Symposium on System Integration*, 2016, pp. 453–458.
- [25] M. Shridhar, L. Manuelli, and D. Fox, “Perceiver-actor: A multi-task transformer for robotic manipulation,” in *Conf. on Robot Learning*, 2023, pp. 785–799.
- [26] A. Goyal, J. Xu, Y. Guo, V. Blukis, Y.-W. Chao, and D. Fox, “Rvt: Robotic view transformer for 3d object manipulation,” in *Conf. on Robot Learning*, 2023, pp. 694–710.
- [27] D. A. Cohn, Z. Ghahramani, and M. I. Jordan, “Active learning with statistical models,” *Journal of artificial intelligence research*, vol. 4, pp. 129–145, 1996.
- [28] H. Pham and Q.-C. Pham, “A new approach to time-optimal path parameterization based on reachability analysis,” *IEEE Trans. on Robotics*, vol. 34, no. 3, pp. 645–659, 2018.
- [29] S. Calinon, F. D’halluin, E. L. Sauser, D. G. Caldwell, and A. G. Billard, “Learning and reproduction of gestures by imitation,” *IEEE Robotics & Automation Magazine*, vol. 17, no. 2, pp. 44–54, 2010.
- [30] J. R. Hershey and P. A. Olsen, “Approximating the kullback leibler divergence between gaussian mixture models,” in *IEEE Int. Conf. on Acoustics, Speech and Signal Processing*, vol. 4, 2007, pp. IV–317.
- [31] T.-W. Ke, N. Gkanatsios, and K. Fragkiadaki, “3d diffuser actor: Policy diffusion with 3d scene representations,” *arXiv preprint arXiv:2402.10885*, 2024.
- [32] C. Chi, S. Feng, Y. Du, Z. Xu, E. Cousineau, B. Burchfiel, and S. Song, “Diffusion policy: Visuomotor policy learning via action diffusion,” in *Proc. of Robotics: Science and Systems (RSS)*, 2023.
- [33] S. Hochreiter and J. Schmidhuber, “Long short-term memory,” *Neural computation*, vol. 9, no. 8, pp. 1735–1780, 1997.
- [34] A. Kirillov, E. Mintun, N. Ravi, H. Mao, C. Rolland, L. Gustafson, T. Xiao, S. Whitehead, A. C. Berg, W.-Y. Lo *et al.*, “Segment anything,” in *Proc. of the IEEE Conf. on Computer Vision and Pattern Recognition*, 2023, pp. 4015–4026.
- [35] J. Gu, F. Xiang, X. Li, Z. Ling, X. Liu, T. Mu, Y. Tang, S. Tao, X. Wei, Y. Yao *et al.*, “Maniskill2: A unified benchmark for generalizable manipulation skills,” in *Int. Conf. on Learning Representations*, 2022.

The Art of Imitation: Learning Long-Horizon Manipulation Tasks from Few Demonstrations

- Supplementary Material -

Jan Ole von Hartz, Tim Welschehold, Abhinav Valada, and Joschka Boedecker

S.1. ADDITIONAL GMM DETAILS

A. Full GMR Equations

For inference, we employ Gaussian Mixture Regression (GMR) [27] to estimate $p_{\mathcal{G}}(\mathcal{O} | \mathcal{I})$. Let

$$\boldsymbol{\mu}_k = \begin{pmatrix} \boldsymbol{\mu}_k^{\mathcal{I}} \\ \boldsymbol{\mu}_k^{\mathcal{O}} \end{pmatrix} \text{ and } \boldsymbol{\Sigma}_k = \begin{pmatrix} \boldsymbol{\Sigma}_k^{\mathcal{I}\mathcal{I}} & \boldsymbol{\Sigma}_k^{\mathcal{I}\mathcal{O}} \\ \boldsymbol{\Sigma}_k^{\mathcal{O}\mathcal{I}} & \boldsymbol{\Sigma}_k^{\mathcal{O}\mathcal{O}} \end{pmatrix}$$

be the partition of $\boldsymbol{\mu}_k$ and $\boldsymbol{\Sigma}_k$ into the input and output dimensions. Then, for $i \in \mathcal{I}$ and $o \in \mathcal{O}$, we have:

$$p_{\mathcal{G}}(o | i) = \sum_{k=1}^K \pi_k^i \cdot \mathcal{N}(o | \boldsymbol{\mu}_k^{o|i}, \boldsymbol{\Sigma}_k^{o|i}), \quad (\text{S.1})$$

where

$$\begin{aligned} \pi_k^i &= \frac{\mathcal{N}(i | \boldsymbol{\mu}_k^{\mathcal{I}}, \boldsymbol{\Sigma}_k^{\mathcal{I}})}{\sum_{l=1}^K \mathcal{N}(i | \boldsymbol{\mu}_l^{\mathcal{I}}, \boldsymbol{\Sigma}_l^{\mathcal{I}})} \\ \boldsymbol{\mu}_k^{o|i} &= \boldsymbol{\mu}_k^o + \boldsymbol{\Sigma}_k^{oi} (\boldsymbol{\Sigma}_k^{ii})^{-1} (i - \boldsymbol{\mu}_k^i) \\ \boldsymbol{\Sigma}_k^{o|i} &= \boldsymbol{\Sigma}_k^{oo} - \boldsymbol{\Sigma}_k^{oi} (\boldsymbol{\Sigma}_k^{ii})^{-1} \boldsymbol{\Sigma}_k^{io}. \end{aligned} \quad (\text{S.2})$$

B. Task Parameterization

The order of marginalization, Eq. (5), transformation, Eq. (6), product, Eq. (7), and GMR, Eq. (2), can be altered. Some authors perform GMR *per* marginal and then join the predicted Gaussians [10]. However, the order proposed here facilitates the sequencing of HMMs, that we introduce in Sec. IV-D.

S.2. ADDITIONAL MANIFOLD DETAILS

A. \mathcal{S}^3 Logarithmic Map

Zeestraten [10] proposes to use the following logarithmic map for \mathcal{S}^3

$$\text{Log}_e(\mathbf{g}) = \begin{cases} \arccos^*(q_0) \frac{\mathbf{q}}{\|\mathbf{q}\|} & , q_0 \neq 1 \\ \begin{bmatrix} 0, 0, 0 \end{bmatrix}^T & , q_0 = 1. \end{cases} \quad (\text{S.3})$$

Here, q_0 denotes the quaternion's real part. They further define

$$\arccos^*(\rho) = \begin{cases} \arccos(\rho) - \pi & , -1 \leq \rho < 0 \\ \arccos(\rho) & , 0 \leq \rho \leq 1. \end{cases} \quad (\text{S.4})$$

This part-wise definition addresses the double-covering of rotations by \mathcal{S}^3 so that antipodal rotations on \mathcal{S}^3 have zero distance in tangent space. However, it introduces discontinuities at $\rho = 0$, which we found problematic when trying to find local near-linear segments. Instead, we use the standard arccos function and preprocess our quaternion data to ensure continuity such that no two successive rotations are antipodal.

B. \mathcal{S}^n Frame Transformation

Recall from Sec. III-D that for a given instance of task parameters $\Theta = \{\mathbf{A}_f, \mathbf{b}_f\}_{f=1}^F$, we transform the per-frame marginals to the world frame using Eq. (6). However, Eq. (6) only applies to Euclidean Gaussians. In contrast, for Riemannian Gaussians [10], we have

$$\hat{\boldsymbol{\mu}}_k^f = \text{Exp}_{\mathbf{b}_f} \left(\mathbf{A}_f \text{Log}_e \left(\boldsymbol{\mu}_k^f \right) \right) \quad (\text{S.5})$$

$$\hat{\boldsymbol{\Sigma}}_k^f = \left(\mathbf{A}_f \boldsymbol{\Sigma}_k^f \mathbf{A}_f^T \right)_{\parallel_{\mathbf{b}_f}^{\hat{\boldsymbol{\mu}}_k^f}}. \quad (\text{S.6})$$

The subscript $\parallel_{\mathbf{b}_f}^{\hat{\boldsymbol{\mu}}_k^f}$ denotes the *parallel transport* of the covariance matrix from $\boldsymbol{\mu}_k^f$ to $\hat{\boldsymbol{\mu}}_k^f$ using \mathbf{b}_f [10]. We discuss the role of parallel transport in more detail in Sec. S.3. For \mathcal{S}^3 we follow prior work [10] and transform the quaternion manifold using $\mathbf{A}_f = \mathbf{I}_3$ and $\mathbf{b}_f = \mathbf{q}_f$, where \mathbf{q}_f is the rotation quaternion that is equivalent to the rotation matrix \mathbf{A}_f . Recall that we use the \mathcal{S}^2 manifold to model the direction of actions (velocities). To enable applying the same frame transformation as for \mathcal{S}^3 , we modify the tangent action function to accept quaternion arguments. Note that any element $\mathbf{p} \in \mathcal{S}^2$ represents a three-dimensional vector of the unit norm, which we can represent as a vector quaternion $[0, \mathbf{p}]^T \in \mathcal{S}^3$. In this way, we can rotate a manifold element $\mathbf{p} \in \mathcal{S}^2$ by a quaternion $\mathbf{q} \in \mathcal{S}^3$ via

$$[0, \hat{\mathbf{p}}]^T = \mathbf{q} [0, \mathbf{p}]^T \mathbf{q}^{-1}, \quad (\text{S.7})$$

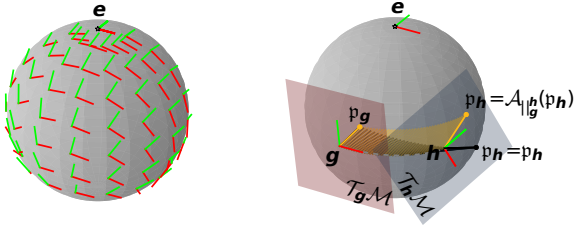
i.e., we embed the vector in \mathcal{S}^3 , compute the Hamilton product, and drop the leading zero to map the resulting vector quaternion back, s.t. $\hat{\mathbf{p}} \in \mathcal{S}^2$. Parallel transport moves an element \mathbf{p}_g of the manifold from one tangent base \mathbf{g} to another \mathbf{h} . Specifically, $\parallel_{\mathbf{b}_f}^{\hat{\boldsymbol{\mu}}_k^f}$ moves $\boldsymbol{\mu}_k^f$ from the base \mathbf{e} , which is the identity element of the manifold, to \mathbf{b}_f , yielding $\hat{\boldsymbol{\mu}}_k^f$. As $\mathbf{b}_f \notin \mathcal{S}^2$, we first need to define a surrogate element to use as the new base. We define

$$\hat{\mathbf{b}}_f = \left(\mathbf{q}_f [0, \mathbf{e}]^T \mathbf{q}_f^{-1} \right)_{[1:3]} \quad (\text{S.8})$$

and substitute $\hat{\mathbf{b}}_f \in \mathcal{S}^2$ for $\mathbf{b}_f \in \mathcal{S}^3$ in Eq. (S.6). Moreover, the exponential map in Eq. (S.5) depends on the base at which it is applied. For homogeneous manifolds, such as \mathcal{S}^n , it can be defined as

$$\text{Exp}_{\mathbf{g}}(\mathbf{p}_g) = \mathcal{A}_e^g(\text{Exp}_e(\mathbf{p}_g)), \quad (\text{S.9})$$

where \mathbf{p}_g denotes the tangent element associated with the manifold element \mathbf{p}_g . $\mathcal{A}_g^h(\mathbf{p}_g)$ denotes the action function [10],



(a) Tangent space alignment w.r.t. e . (b) Base misalignment between g and h .

Fig. S.1: Parallel transport of the manifold element p from basis g to basis h requires a rotation by $\mathcal{A}_{g,h}(p)$ to compensate for the misaligned tangent spaces. Source: Adapted from [10].

which maps p_g to p_h along a geodesic, such that pairwise distances between both p_g and g , and p_h and h are identical. As $\mathcal{A}_g^h(p_g)$ requires g to be a manifold element, we again leverage Eq. (S.7) to calculate

$$\text{Exp}_{\tilde{b}_f}(p_g) = \mathcal{A}_e^{\tilde{b}_f}(\text{Exp}_e(p_g)) \quad (\text{S.10})$$

$$\left[0, \mathcal{A}_e^{\tilde{b}_f}(p_g)\right]^T = q_f \left[0, p_g\right]^T q_f^{-1}. \quad (\text{S.11})$$

For reference, the quaternion action on \mathcal{S}^3 is similarly defined as

$$\mathcal{A}_g^h(p_g) = h g^{-1} p_g \quad (\text{S.12})$$

$$\mathcal{A}_e^{\tilde{b}_f}(p_g) = q_f p_g. \quad (\text{S.13})$$

Putting the modified parallel transport and action together, for \mathcal{S}^2 we have

$$\hat{\mu}_k^f = \text{Exp}_{\tilde{b}_f} \left(\mathcal{A}_f \text{Log}_e \left(\mu_k^f \right) \right) \quad (\text{S.14})$$

$$\tilde{\Sigma}_k^f = \left(\mathcal{A}_f \Sigma_k^f \mathcal{A}_f^T \right)_{\parallel \hat{\mu}_k^f}, \quad (\text{S.15})$$

with \hat{b}_f and $\text{Exp}_{\tilde{b}_f}$ as defined in Eq. (S.8) and Eq. (S.11), respectively.

S.3. COVARIANCE REGULARIZATION

During EM, the model might learn unwanted correlations between some of the data dimensions. This well know problem can lead to faulty predictions, as illustrated in Fig. S.2a. Usually, this issue can be solved using shrinkage regularization in EM [10]. However, we found the regularization of the EM to be sometimes insufficient to ensure high quality predictions in Riemannian TP-GMMs. Specifically, the transformation of the local marginal models can re-add unwanted correlations. To the best of our knowledge, this fact was not reported in prior work, so we discuss it in this section.

Consider a Riemannian TP-GMM on the manifold $\mathcal{M} = \mathbb{R} \times \mathbb{R}^3 \times \mathcal{S}^3$, modeling time, as well as position and rotation of the end-effector. Note that for the rotation quaternion, the covariance matrix is defined and computed in the tangent space $\mathcal{T}_x \mathcal{S}^3$. Thus, it is given by a 3×3 matrix. Recall the frame transformation of the marginal models discussed in Sec. III-D. While regularization of EM can dampen or remove unwanted correlations, the frame transformation can

add novel correlations back in, as shown in Fig. S.2b. Perhaps surprisingly, the culprit is *not* the transformation of the covariance matrix in Eq. (6). While it clearly changes the correlations between the (Euclidean) position dimensions x, y, z , the novel correlation between the rotation dimensions qx and qy hails elsewhere.

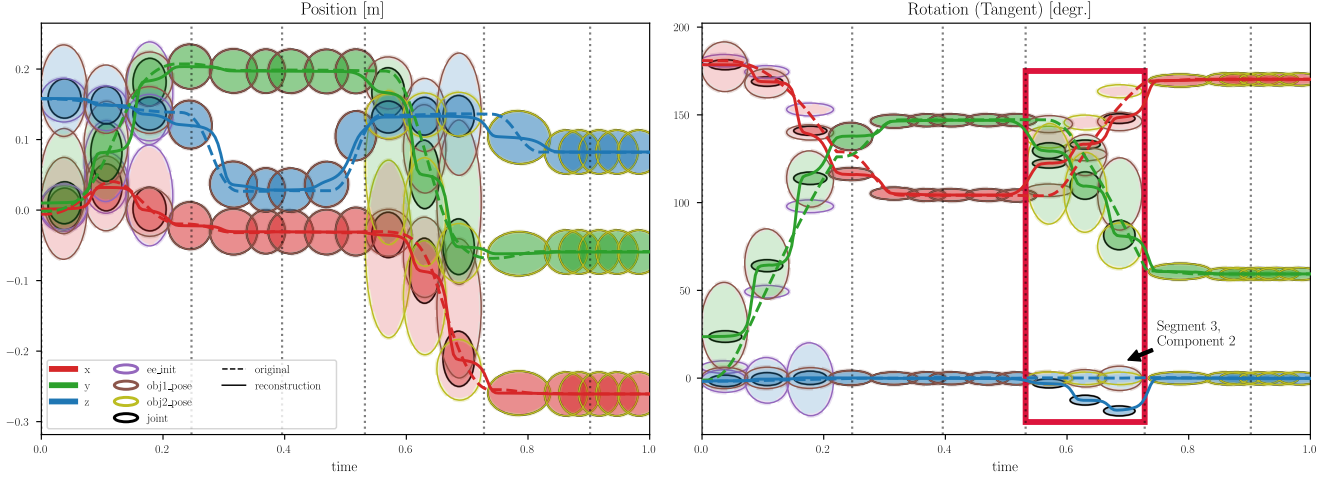
Riemannian TP-GMMs use *parallel transport* to implement frame transformations [10]. Parallel transport moves a Gaussian from its current tangent basis (mean) to a new tangent basis along the connecting geodesic, as shown in Fig. S.1b. Following the geodesic ensures compensation for the relative rotation between the old and new tangent space, indicated in Fig. S.1a. In practice, this is implemented by first shifting the mean of the Gaussian to its new position, and then applying the compensating rotation matrix to the covariance matrix [10]. This rotation of the covariance matrix introduces novel correlations. For illustration, we have heavily regularized the marginal covariance matrix in Fig. S.2b before transforming it. It does not contain any correlation between the rotation dimensions. Note how the frame transformation adds in additional correlations between the rotation dimensions qx and qy , leading to the faulty reconstruction in Fig. S.2a. Fig. S.2c shows the same transformed covariance, but omits the compensating rotation of the tangent space. Crucially, it does not contain any correlation between qx and qy .

The reconstruction of qz is also affected because of two reasons. First, recall the product of marginal models in Eq. (7). If another marginal correlates, for example, qy and qz due to a different frame transformation, then in the joint model, all three rotation dimensions are now correlated. This might be, why previous work computed the GMR per marginal and only joint the predicted Gaussians [10]. However, combining the marginals first, homogenizes the input dimensions of GMR, thus simplifying the cascading of models, discussed in Sec. IV-D. Second, the rotation dimensions interact because of the Manifold structure of \mathcal{S}^3 . The tangent space of the quaternion manifold can be interpreted as representing the rotation axis, scaled by half the rotation angle [10]. Consequently, all dimensions interact with each other when mapping back and forth using the exponential and logarithmic maps. To solve this problem, we apply an additional diagonal regularization after the frame transformation (parallel transport). Fig. S.2d shows the new covariance matrix and Fig. S.2e the corrected reconstruction. Other regularization schemes are possible, such as allowing correlations between the time and position dimensions. Because positions are Euclidean, they do not suffer from the same problem introduced by parallel transport. Note that such regularization also removes some of the desired correlations from the model, as can be seen from the missing rotation of the Gaussians in Fig. S.2e.

S.4. EXPERIMENTAL DETAILS

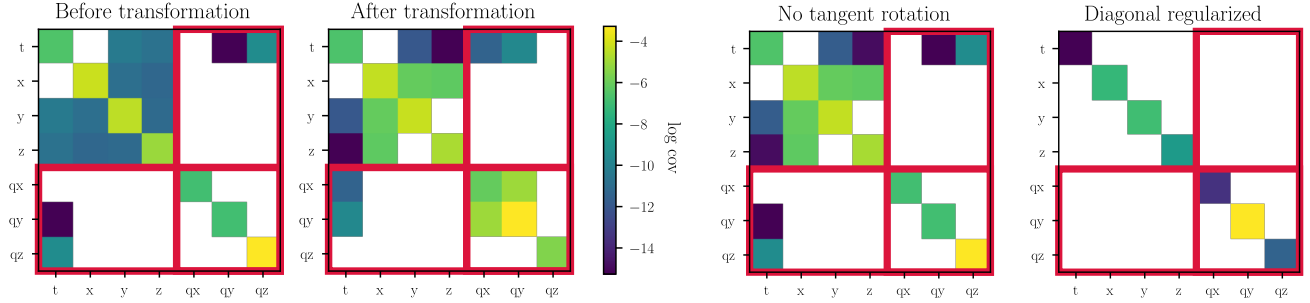
A. Baseline Hyperparameters

For Diffusion Policy, we closely follow Chi *et al.* [32] in the selection of the hyperparameters. We perform receding horizon control on absolute end-effector poses with an observation horizon of two and an action horizon of eight.



(a) Faulty reconstruction due to unwanted correlations. The plot shows the model dimensions over time. Left: position as x, y, z coordinates. Right: rotation in tangent space as scaled axis-angle components qx, qy, qz . Vertical dotted lines indicate the borders of the segment models. Red, green, and blue represent the individual components. The ellipses with colored borders represent the transformed marginals. The ones with black borders represent the joint model, which is the product of the marginals. Note how the rotation reconstruction is faulty around $t = 0.6$. Note further, how at the same time the blue joint Gaussians are shifted down from where one would expect them.

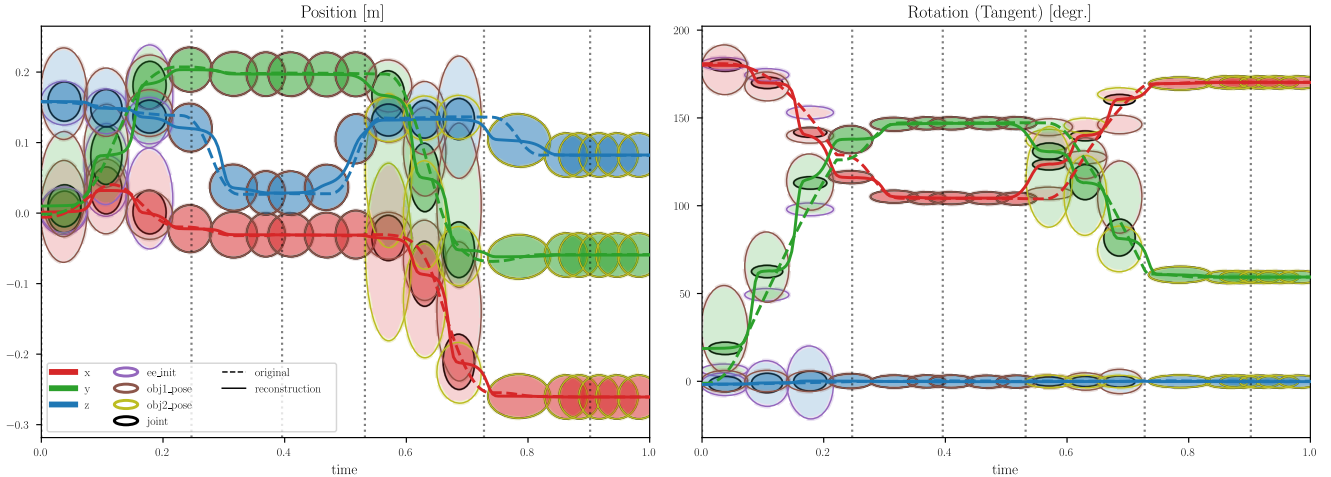
Segment 3, Component 2



(b) Log covariance of segment 3, component 2 of the marginal model of $obj1$ - before and after transformation. White values are near $-\infty$. t indicates time, x, y, z position, qx, qy, qz rotation. Note how the transformation adds in additional correlations for the rotation dimensions.

(c) Without tangent rotation. Note that there are no novel correlations between the rotation dimensions.

(d) Diagonal regularization removes the novel unwanted correlations between the rotation dimensions.



(e) Fixed reconstruction after applying the additional diagonal regularization after the parallel transport of the covariance matrices. Note how the joint model's Gaussians for the rotation dimensions are now located at the expected positions.

Fig. S.2: Frame transformations introduce unwanted correlations, causing faulty reconstructions. Subfig. a shows a faulty reconstruction for the rotation. This is caused by the correlations introduced by the frame transformation shown in Subfig. b. Subfig. c highlights that this is a direct consequence of the rotation $\mathcal{A}_{\parallel g}^h(p)$ explained in Fig. S.1. To remedy this issue, we apply an additional diagonal regularization after the parallel transport. Subfig. d shows the new covariance matrix and Subfig. e the fixed reconstruction.

We also adopt the proposed cosine learning rate schedule. However, when training on only five demonstrations, we reduce the number of warm-up steps from 500 to 50 to account for the reduced duration of the epochs. For a full list of hyperparameters, please see refer to [32] and to the accompanying code repository. For setting up the LSTM, we follow von Hartz *et al.* [4] and utilize a two-layer LSTM to predict end-effector velocities. To improve learning, we transform the task parameters into the gripper frame. For both baselines, we perform linear normalization of both the policy inputs and outputs to improve gradient flow.

B. Skill Segmentation and Parameter Selection

We ablate the skill segmentation and task-parameter selection on three tasks: `SlideBlock`, `OpenDrawer`, and `PlaceCups`. The first two are single-object tasks, but only `OpenDrawer` requires a precise grasping action, while `SlideBlock` does not. `PlaceCups` not only adds multiple task-relevant objects but also additional clutter objects. These three tasks are therefore a representative sample of all tasks. We fit all models using identical hyperparameters.

C. State-Driven Policies

HMM: For this experiment, we slightly modify the Hidden Markov Model. The resetting of the end-effector pose can lead to zero state probabilities across all states. This can easily be seen from Eq. (3), which combines the current state distribution with the transition model and current observation probability. The disturbance of the pose constitutes an unexpected state transition, leading to zero probabilities under the new observation. Multiple possibilities exist to remedy this issue, such as allowing all state transitions with some

small probability. For simplicity, we allow the model to reset the prior $\pi_k^{i_t}$ when all state probabilities become zero.

Disturbance: We disturb the policies by freezing the end-effector for 90 timesteps in `SlideBlock` and 250 timesteps in `LiftBottle`. The duration has been selected to correspond to the first contact point with the task object, such that the policies need to recover during a challenging part of the task. We freeze the end-effector for n time steps, rather than resetting its pose after n steps, as resetting the pose directly can sometimes allow a state-based HMM that got stuck in a specific state to recover and we did not wish to mix these different effects.

D. Real-World Policy Learning

We use a single wrist-mounted Intel Realsense D435 camera to provide RGB-D observations. We estimate the keypoint locations in 2D as described in [4], [12] and project them to 3D using the depth channel of the camera. For each task, we manually select a set of five candidate task parameters on scene objects. While automatic sampling from SAM-generated masks works well, manual sampling takes less than 30 seconds per task and allows for additional user control. In particular, it allows us to ensure that the set of candidates represents a mix of task-relevant objects and clutter objects to challenge our task-parameter selection. For example, in the `PickAndPlace` task, the policy needs to pick up a banana from a cutting board and place it in a bowl. We select one candidate each on the banana, on the bowl, on the cutting board, on a cutter knife, and on the table. Only the first two are relevant to the task, whereas the other three are distractors. We also show an example of this procedure in the supplementary video.